




Comparison of Mo and ITO back contacts in CIGSe solar cells: Vanishing of the main capacitance step

Thomas Schneider | Christiane Dethloff | Torsten Hölscher  | Heiko Kempa  | Roland Scheer 

Institute of Physics, Martin-Luther-University Halle-Wittenberg, Halle (Saale), Germany

Correspondence

Heiko Kempa, Institute of Physics, Martin-Luther-University Halle-Wittenberg, von-Danckelmann-Platz 3, 06120 Halle (Saale), Germany.

Email: heiko.kempa@physik.uni-halle.de

Funding information

Bundesministerium für Bildung und Forschung, Germany, Grant/Award Number: 03EK3570B

Abstract

Admittance measurements of Cu (In, Ga)Se₂ (CIGSe) solar cells typically show at least one capacitance step, the so-called N1 signal. Its origin is still under debate, even though the signal is present in almost all CIGSe solar cells. In this work, CIGSe solar cells with different absorber layer thicknesses have been prepared on Mo and on indium tin oxide (ITO)-based back contacts. The samples were analyzed by temperature-dependent current–voltage (JV) and admittance measurements. No N1 signal was found for ITO-based samples. The N1 signal was also absent in Mo-based solar cells with an ultrathin absorber layer, unless a forward bias voltage was applied. The observations can be consistently explained by a back contact barrier, which is only present in the Mo-based solar cells. The explanation is further supported by measured JV curves and by theoretical simulations. The results give a strong indication that the N1-signal is due to a back contact barrier. While a back contact barrier is not necessarily detrimental for regular CIGSe solar cells, it may be an issue for CIGSe solar cells with ultrathin absorbers, where a so-called punch-through effect can occur.

KEYWORDS

admittance spectroscopy, CIGSe solar cells, Schottky contact

1 | INTRODUCTION

Admittance measurements are an important tool to analyze various properties of semiconductors including doping and defect densities. However, the analysis of admittance spectra is challenging. Due to similar effects on the spectra, transport barriers can be mistaken as defects and vice versa. Interestingly, admittance measurements on Cu (In, Ga)Se₂ (CIGSe)-based solar cells basically always show at least one capacitance-frequency step, which is commonly referenced as the so-called N1-signal. Despite 30 years of research, there is still an ongoing debate on its origin.^{1,2} It was often interpreted as a shallow defect

with an activation energy in the range of 50 to 150 meV, typically located close to the absorber/buffer interface.³ An alternative explanation involves a hole extraction barrier at the back contact.^{1,4} The presence of a back contact barrier for CIGSe solar cells was concluded by several authors.^{5,6} It can lead to a counter diode in relation to the main junction. The effect on solar cell parameters under normal operation conditions may well be negligible for not too large a back contact barrier height.⁵

A back contact barrier, however, can become important in the case of ultrathin solar cells. When the calculated width of the space charge region of the main junction approaches the absorber thickness,

This is an open access article under the terms of the Creative Commons Attribution-NonCommercial-NoDerivs License, which permits use and distribution in any medium, provided the original work is properly cited, the use is non-commercial and no modifications or adaptations are made.

© 2021 The Authors. Progress in Photovoltaics: Research and Applications published by John Wiley & Sons Ltd.

the open-circuit voltage becomes dependent on the work function of the back contact metal: simulations show that the built-in-voltage decreases if the work function decreases.⁷ This effect was found for CdTe solar cells even with regular absorber thickness due to the typically low doping densities in CdTe. In this case, it is discussed as a so-called reach-through or punch-through diode.⁷ For CIGSe solar cells, it could be present in the case of very thin absorber layers (<500 nm).

For this work, the standard Mo back contact was replaced by indium tin oxide (ITO). Several n-type oxides have been successfully used as the electrical back contact for CIGSe solar cells despite effectively creating an n-p-n structure.⁸ Transparent conductive oxides like ITO serve as back contacts for bifacial solar cells.^{8–12} Recently, they also became of interest for light management applications.^{9,11–17} CIGSe solar cells with different absorber layer thicknesses and with ITO or Mo back contacts were studied recently in order to determine the back contact recombination velocity at the CIGSe/ITO interface from bifacial measurements combined with systematic simulations.¹⁸ For the present work, we used the very same samples as in Schneider et al.¹⁸ to investigate the influence of the back contact on admittance spectra. Additionally, capacitance-voltage (CV), drive-level capacitance profiling (DLCP), and temperature-dependent current-voltage (JV) measurements were performed. We show that the results of these experiments provide strong evidence that the N1 signal is related to a back contact barrier, which is present in CIGS solar cells with Mo back contact, but absent in samples with ITO back contact.

2 | EXPERIMENTAL DETAILS

Solar cells were prepared on two different types of back contacts. One of the back contacts was deposited by sputtering 260 nm of ITO on commercially available 2.1-mm-thick soda-lime glass (SLG) substrates covered with a 110-nm SiN_x layer to prevent Na diffusion from the SLG during absorber preparation. The sheet resistance of the ITO layer was 7 Ω/sq as determined by four-point measurements. The sheet resistance was measured on completed solar cells, where the layers above the ITO-back contact were removed mechanically. The other back contact was commercially deposited Mo on 3-mm-thick SLG, also with a 200-nm SiO_xN_y barrier against Na diffusion. The following steps were processed always simultaneously on both back contact types. CIGSe layers of three different thicknesses (300 nm, 550 nm, and 1020 nm) were deposited using thermal evaporation in a three-stage process. The maximum substrate temperature was 480°C for all processes. We note, however, that the substrate temperature was measured at the back side of the substrate; therefore, the actual growth temperature of the CIGSe layer can differ, especially between the two back contact types due to their different emissivity and the different thickness of the substrates. Hence, the possibility of CIGSe layer properties depending on the back contact must be taken into account when interpreting experimental results.

Directly after the absorber preparation, 2 nm of NaF, as predetermined by flux measurements, was deposited inside the same

vacuum chamber at a substrate temperature of 450°C using thermal evaporation. Subsequently, a buffer layer of approximately 50 nm of CdS was applied using chemical bath deposition. The window layer was deposited by sputtering 140 nm of intrinsic ZnO followed by 210 nm of ITO. Finally, a metal grid consisting of Ni/Al/Ni layers was deposited by electron beam evaporation through a shadow mask. Solar cells of approximately 45 mm² were defined by chemical etching of the front contact. To this end, 10% HCl was applied using a fine paint brush to the front surface, locally removing the ITO/ZnO/CdS layers without any masking.

The finished solar cells were characterized by JV measurements at room temperature using a home-built sun simulator with a halogen lamp. The light intensity of the lamp was adjusted by matching the current of a Si reference solar cell to the current anticipated under AM1.5G conditions. Furthermore, temperature-dependent JV and impedance measurements were carried out in a cryostat chamber. Mo and ITO-based samples with the same absorber layer thickness were measured simultaneously side by side. Before each impedance and dark JV measurement, the samples were relaxed in the dark at an elevated temperature for several hours. The sample temperature was measured individually for each sample. Temperature-dependent measurements were performed starting at 80 K followed by a temperature increase in 10 K steps. A xenon light source was used for the temperature-dependent JV curves with the light intensity adjusted identically to the halogen lamp. The impedance measurements were performed using an Agilent E4980A LCR meter. The AC signal amplitude was 30 mV throughout all measurements. DLCP and CV measurements have been conducted at measurement frequencies of 5 kHz and 50 kHz. In order to reduce the influence of the series resistance, the cell area was reduced to approximately 20 mm² for the impedance measurements. For comparison, impedance simulations were carried out in 1D using the software AFORS-HET.¹⁹

The chemical composition of the absorber layer was determined on Mo reference samples using energy-dispersive X-ray spectroscopy (EDX). The GGI depth profile was determined using glow discharge optical emission spectroscopy (GDOES) with a GDA 750 of Spectra Analytik.

3 | RESULTS AND DISCUSSION

3.1 | Chemical composition

The $GGI = [Ga]/([In] + [Ga])$ and $CGI = [Cu]/([In] + [Ga])$ values obtained from EDX measurements are given in Table 1. It must be noted that the Mo back contact was visible in the EDX measurements

TABLE 1 GGI and CGI from EDX measurements

Absorber layer thickness (nm)	300	550	1020
CGI	0.80	0.78	0.79
GGI	0.37	0.32	0.33

for absorber thicknesses below 1.1 μm . Therefore, a higher error is expected for thinner absorber layers. Within this error, no difference in the overall absorber composition between Mo-based and ITO-based samples was observed.

The GGI depth profiles measured with GDOES are displayed in Figure 1 together with the Na concentration profiles. All GGI profiles exhibit a notch, which is typically observed for samples from a three-stage process. The width of this notch is increasing with the absorber thickness. The GGI notch minimum is least pronounced for the thinnest absorber thickness; that is, the notch is not as deep. The notch is slightly more pronounced in the case of the ITO-based samples. This difference is most likely caused by a different mobility of Ga and In during the absorber deposition. The different mobility can be either due to a different preferred crystal orientation of the CIGS caused by the different back contact types or due to a different sample temperature during the layer growth. The difference in process temperature is most likely also responsible for the small differences in the Na profiles.

A decrease of the GGI close to the back contact was reported in Keller et al.¹² for (Ag, Cu)(In, Ga)Se₂ solar cells grown on hydrogen-doped In₂O₃ back contacts. The formation of Ga₂O₃ close to the back contact was found as the origin and Na(F) was discussed to promote the formation of Ga₂O₃. The observed reduction of the GGI close to the back contact found in Figure 1 can be explained by the onset of the ITO back contact. The absence of Na during the CIGSe deposition might have helped to avoid excessive formation of Ga₂O₃. However, a thin layer of Ga₂O₃ is expected, which cannot be determined by the limited spatial resolution of the GDOES.

Interestingly, the Na concentration also shows a notch with its minimum position roughly at the same position as the GGI notch. The minimum Na concentration is becoming smaller with increasing absorber layer thickness. The Na concentration strongly increases towards the front and the back contact. The Na front gradient can be

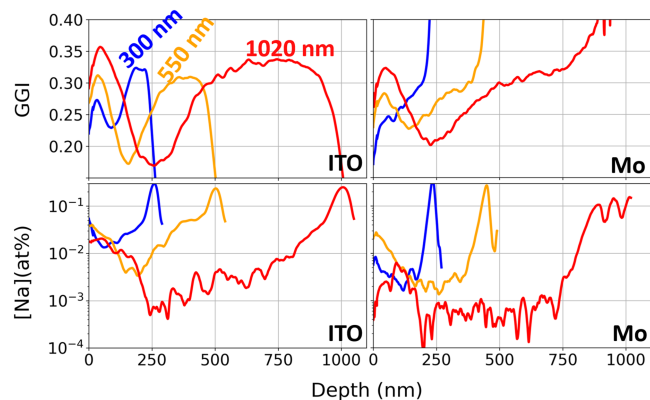


FIGURE 1 GDOES data for the different CIGSe absorber layer thicknesses on ITO back contacts (left column) and on Mo back contacts (right column). The upper row shows the GGI, while the lower row shows the Na content in atomic percent. The dashed lines mark the positions, where the Mo signal reaches 1 at% for the Mo-based samples as an estimation of the onset of the back contact

expected, because Na was introduced into the sample solely by deposition of NaF on the front interface of the absorber layer. Hence, Na near the back contact originates from diffusion through the absorber layer. The gradient towards the back can be explained either by a reduced Na diffusivity at the CIGSe/back contact interface leading to a pile-up or by an enhanced density of grain boundaries close to the back contact since Na is typically found at the grain boundaries of CIGSe.²⁰

In view of the minor differences of the absorber layers on both back contact types, a different chemical composition of the absorber can be ruled out as origin of the different appearance of the N1 signal.

3.2 | Solar cell characterization

Figure 2 shows the JV curves of solar cells with both back contact types and different absorber layer thicknesses. The extracted solar cell parameters are given in Table 2. Herein, only the best solar cells are shown for each sample type. Measurements of the external quantum efficiency and optical calculations using the transfer matrix method are given in the supplemental material.

Except for the 550-nm sample, the Mo-based solar cells exhibit higher fill factors (FF), which can be explained by a higher series resistance in case of the ITO-based samples due to the lower conductivity of ITO in comparison with Mo. However, both open-circuit voltages (V_{OC}) and short circuit currents (J_{SC}) are larger in case of the ITO-based samples, resulting in higher power conversion efficiencies (PCE) in comparison with the Mo-based samples except for the samples with the highest absorber thickness. Both V_{OC} and J_{SC} become smaller with decreasing absorber layer thickness; however, the V_{OC} decrease is more pronounced in case of the Mo-based samples. The stronger V_{OC} effect of Mo-based cells can have different reasons: It may be related to different back contact recombination rates or possibly different absorber qualities due to a different layer growth induced by the back contact or by a difference in the sample temperature.

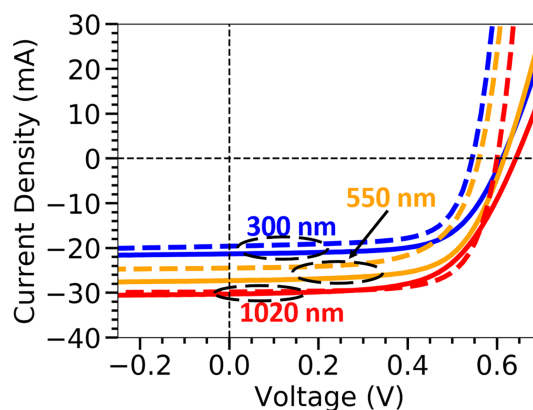


FIGURE 2 JV curves of solar cells with Mo (dashed lines) and ITO (full lines) back contacts and with three different absorber layer thicknesses

Alternatively, the stronger V_{OC} decrease of the Mo-based samples may be related to the punch-through effect due to the presence of a back contact barrier (see below).

3.3 | Temperature-dependent JV measurements

Figure 3 shows JV curves with and without illumination measured at temperatures ranging from 80 K to 330 K. In the case of the Mo-based samples a kink in the first quadrant of the illuminated JV curves becomes increasingly visible with decreasing temperature. It is less pronounced for the 300-nm sample.

TABLE 2 Solar cell parameters for the different back contact types and absorber layer thicknesses

Back contact	V_{OC} (mV)	FF (%)	J_{SC} (mA/cm ²)	PCE (%)
d (CIGSe) = 300 nm				
Mo	544	68.9	19.6	7.3
ITO	611	65.5	21.3	8.5
d (CIGSe) = 550 nm				
Mo	560	63.9	24.5	8.7
ITO	616	65.0	27.3	10.9
d (CIGSe) = 1020 nm				
Mo	605	72.0	29.8	13.0
ITO	642	61.3	30.3	11.9

Note: The J_{SC} values are determined using EQE measurements, while the other parameters are extracted from JV curves.

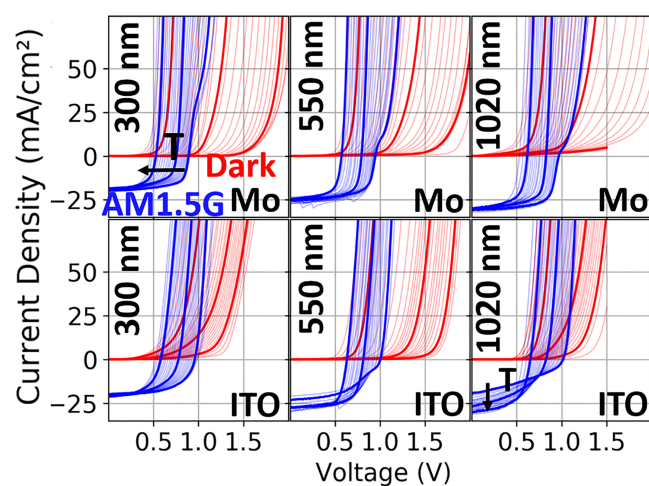


FIGURE 3 Temperature-dependent JV curves measured in dark (red) and under illumination (blue) for the different absorber layer thicknesses and back contact types. The curves are plotted with thick lines for 100 K, 200 K, and 300 K. The black arrows show the relative shifting direction of the JV curves with increasing temperature. The temperature ranges between 80 K and 330 K in 10 K steps

The presence of a kink in JV curves is sometimes explained by a large cliff at the buffer/window interface leading to a blocking of the diode current under large forward bias.²¹ An alternative explanation would be that the observed kink is caused by a back contact barrier limiting the diode current transport. The conductivity might increase under sufficient forward bias due to a breakdown of the back contact barrier or an increased tunneling through the back contact barrier as proposed by Ledinek et al.²² This approach could also explain why the kink was only observed for the Mo samples, given the assumption that no back contact barrier is present in the ITO-based samples.

Both sample types exhibit a strong cross-over between illuminated and dark JV curves, especially at lower temperatures, which is more pronounced in case of the Mo-based samples. According to literature, such a cross-over can result from a barrier at the CIGSe/CdS interface, which disappears under illumination due to enhanced effective doping of the CdS layer,²³ or from a back contact barrier.²⁴ Hence, the (additional) presence of a back contact barrier can explain the stronger cross-over in case of the Mo-based samples.

The ITO-based sample with the highest absorber thickness of 1020 nm shows another type of distortion. With decreasing temperature, the fill factor as well as J_{SC} decrease. By plotting the normalized J_{SC} as a function of temperature (Figure 4), a tendency of decreasing J_{SC} with decreasing temperature can be seen for the ITO-based samples, albeit some data scattering due to variation of the solar simulator. Apparently, the collection of generated charge carriers is hindered at lower temperatures in the ITO-based samples. We speculate, that this effect might be related to a tunneling barrier, which is building up

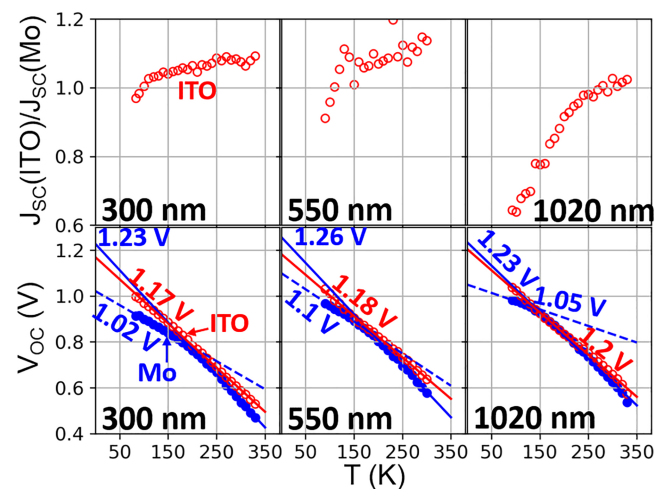


FIGURE 4 Temperature dependence of J_{SC} (upper row) and V_{OC} (lower row). Since J_{SC} is much less temperature-dependent in the Mo-based samples than in the ITO-based samples, J_{SC} of the ITO-based samples is referenced to J_{SC} of the Mo-based samples, the latter thus serving as an approximate measure of the variation of the light intensity. The lines correspond to linear fits of the V_{OC} -curves at low temperatures (dashed lines) and at higher temperatures (full lines), respectively. In case of the ITO-based samples, the whole V_{OC} -measurement range was used for the linear fit. The voltage labels give V_{OC} extrapolated to 0 K

at the back contact with increasing deposition time of the absorber. A possible candidate for such a barrier would be a Ga_2O_3 layer growing at the elevated temperatures during absorber deposition on the ITO back contact.^{8,11,12,15} There are indications in the literature that an ITO back contact without a Ga_2O_3 forms an ohmic contact.^{25,26}

Figure 4 also shows the open-circuit voltage as a function of the sample temperature. All ITO-based samples exhibit an almost linear increase of V_{OC} with decreasing temperature. The extrapolated values at 0 K between 1.17 and 1.20 eV should, according to the ideal diode equation, correspond to the absorber band gap plus approximately 0.075 V due to temperature dependent parameters.²⁷ This holds true for the Mo-based samples by extrapolating in the high temperature range. However, their $V_{\text{OC}}(T)$ slopes are declining towards lower temperatures. This behavior is typical for CIGSe solar cells with Mo back contacts and can be explained by a back contact barrier. Ott et al. derived the functional dependence $V_{\text{OC}}(T)$ in the presence of a back contact barrier.²⁴ According to their model, $V_{\text{OC}}(T)$ extrapolates to the bandgap plus 0.075 eV at high temperatures. In our samples, this value lies between 1.23 and 1.26 eV. At low temperatures, the model predicts the transition to a different $V_{\text{OC}}(T)$ -slope. This behavior can be clearly recognized in the measurements. An extrapolation to 0 K in the low temperature range should give the band gap of the material reduced by the back contact barrier height. Here, we obtain values between 1.02 and 1.10 eV. The difference between the extrapolated values from the high and the low temperature range (i.e., the back contact barrier height according to the applied model) is 210 meV, 160 meV, and 180 meV in the order of increasing absorber thickness. We note, however, that the barrier height might be underestimated because the slope of the temperature dependence of V_{OC} might still change towards temperatures lower than the ones accessible in our measurement.

3.4 | Charge carrier density

Figure 5 shows the charge carrier density profiles extracted from both CV and DLCP measurements at a frequency of 50 kHz. A comparison with measurements performed at 5 kHz is made in Figure S2, where a stronger frequency dependence is visible in the case of the ITO-based samples compared to the Mo-based samples.

For both sample types similar results were obtained from CV and DLCP measurements, respectively. A typical U-shape can be recognized in all curves except for the CV measurements on Mo-based solar cells. This shape is commonly observed in the apparent carrier density profiles derived from CV measurements.^{1,28} One possible explanation for the increasing carrier density in reverse bias (largest depth) is the charging of deep defect states.²⁹ For the increase in forward bias an explanation involving a back contact barrier was put forward.¹ However, since the increase of the apparent doping density happens also for the ITO back contact, this explanation would require a back contact barrier for both sample types. In a theoretical study, Sozzi et al. showed that the increase of the apparent carrier density in forward and in reverse bias can be explained by the level of the CdS doping density.²⁸ Usually, for the extraction of the charge carrier density from CV measurements a one-sided p-n-junction with highly asymmetric doping is assumed. The simulations in Sozzi et al.²⁸ showed that if the CdS doping is not high enough for such an n^+p -junction, the charge carrier density obtained at the minimum of the U-shape is considerably smaller than the actual doping density, which is instead approached under sufficiently high reverse and forward bias.

In the case of the 1020-nm-thick absorber layer, a slightly lower charge carrier density is measured for the Mo-based solar cells compared with the ITO-based ones. Apart from this, almost no increase of the doping density can be seen for decreasing absorber thickness. This finding is unexpected since the same NaF treatment was applied to all samples and accordingly different Na concentrations, depending on the absorber layer thickness, were found by GDOES measurements in the depth region where the doping density was determined from the CV measurements (see Figure 1). We note, however, that in the case of the 300 nm absorber layer the determined doping densities would lead to an almost complete depletion of the absorber layer. In this case, a different than the actually observed shape of the charge carrier density versus depth plot would be expected. Related simulation results are given in Figure S3, where a steep increase of the determined charge carrier density under reverse bias occurs, roughly when the measurement depth approaches the absorber layer thickness, due to saturation of the capacitance. In contrast, a rather flat CV curve for 300-nm absorber layer thickness and Mo back contact is observed in the measurement with depth values exceeding the absorber layer thickness. Probably the doping density in the absorber

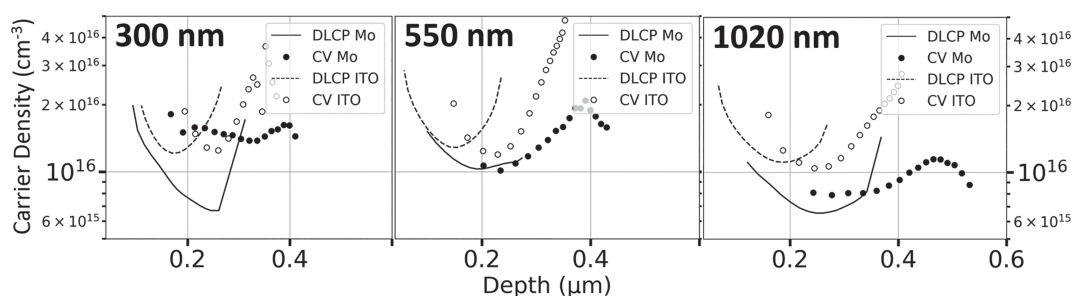


FIGURE 5 Charge carrier density profiles extracted from CV (circle) and DLCP (line) measurements

is underestimated due to doping of either the CdS or the ZnO being not high enough to satisfy the condition that the n-side is much higher doped than the p-side. In conclusion, rather similar CIGSe doping densities are found in CV and DLCP measurements for the Mo-based and ITO-based samples. The densities for the 300 nm CIGSe samples are such that an overlap of the space charge regions of the main and back junctions appears possible, at least under reverse bias.

3.5 | Admittance spectroscopy

Figure 6 exemplarily shows frequency-dependent capacitance curves of the samples with a 550 nm absorber layer thickness for different temperatures at zero bias voltage. The full set of capacitance-frequency curves is given in Figure S4. In case of the Mo-based sample, two capacitance steps are visible, a larger step, which we identify as the N1 signal and a smaller step, denoted as U3, which is only visible at the lowest temperatures. The ITO-based sample also shows the U3 signal, but most importantly, the N1 related large capacitance step is missing. For this sample, another very broad capacitance step at higher temperatures, denoted as U2, can be discerned. An additional feature is the capacitance decrease close to the maximum measurement frequency, especially for the ITO sample. This is likely due to a series resistance, which is not included in the equivalent circuit and thus distorts the capacitance evaluation.³⁰

In order to understand the origins of features in frequency-dependent capacitance curves, it is instructive to study measurements at different bias voltages³¹ and to present the signals in color plots of $-\omega dC/d\omega$ as a function of temperature and angular frequency. Such a family of plots for all sample types is displayed in Figure 7. Note that the color scale was adjusted for each subplot to make the signals clearly visible. The following features can be recognized:

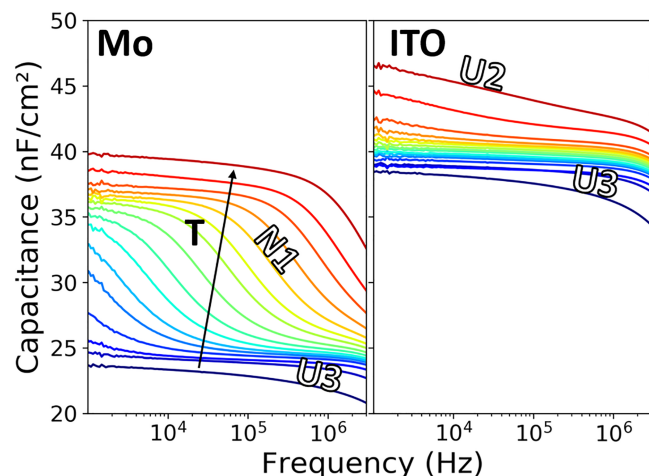


FIGURE 6 Frequency-dependent capacitance measurements at zero bias voltage of solar cells with 550 nm thick absorber layers and Mo and ITO back contacts, respectively. The temperature ranges between 80 K and 250 K in 10 K steps

- N1. This signal is present in all of the Mo-based samples but is absent in all of the ITO-based ones. Its position in the ω -T diagram is virtually independent of the bias voltage applied to a particular solar cell. It shifts to higher temperatures with decreasing absorber thickness. However, the signal disappears in case of the thinnest absorber layer on Mo back contact at zero and reverse bias voltage.
- U1. This feature is clearly visible only for the sample with Mo back contact and 300 nm absorber layer thickness for zero and reverse bias.
- U2. This signal is only present in the samples with ITO back contact and disappears under larger forward bias. The position shifts to higher temperatures under reverse bias. Because of a similar position, this signal may be of the same origin as U1.
- U3. This admittance signature occurs at low temperatures. However, it is generally better visible for the ITO-based samples and under forward bias.

If the N1 signal would be interpreted in the framework of a defect, then it would have to be explained why this defect is missing for the ITO-based samples. The universal appearance of the N1 signal in CIGS layers was demonstrated in numerous publications. Chemical, as well as electronic analysis in Sections 3.1–3.4 revealed great similarities between the ITO- and Mo-based solar cells. Therefore, a complete removal of a defect-related N1 signal by the ITO back contact is unlikely. In contrast, the assumption of a back contact barrier in the Mo-based samples leads to a straightforward explanation of the experimental findings. Under this assumption, the N1 signal arises from the transition between two capacitance regimes: the sole front junction capacitance at low frequency and the series-connection of front and back contact capacitances at high frequency.¹ Also, the disappearance of the N1 signal for the 300-nm Mo-based sample can be explained in this framework. At such low absorber layer thickness, the diodes at the back and at the front interface begin to overlap under reverse bias conditions. In this case of a so-called punch-through, a change in the capacitance regime is not possible anymore. This scenario is supported by simulation results from AFORS-HET, which are shown in Figure 8. Here, the absorber layer thickness was 300 nm, and a back contact barrier of 250-meV height was implemented. Further details are given in the supporting information. Similar to the experiment (Figure 7, first column on the left), no signal is visible at reverse bias and only a small signal appears at zero bias voltage. With increasing forward bias the signal becomes more pronounced due to the reduction of the front junction width, whereby the two diodes become separated again.

Eisenbarth et al. derived a mathematical expression, which links the temperature dependence of the so-called critical frequency with the back contact barrier height.¹ This evaluation is quite similar to the one described by Walter et al. for the evaluation of defect contributions to admittance signals.³² The critical frequency ω_0 is determined by finding the maximum value of a $-\omega d\omega/dC$ versus ω plot. In Appendix A, we show that the barrier height can then be determined from an Arrhenius plot using a $\ln(\omega_0/T^{1.5})$ versus $1/T$ plot in the case

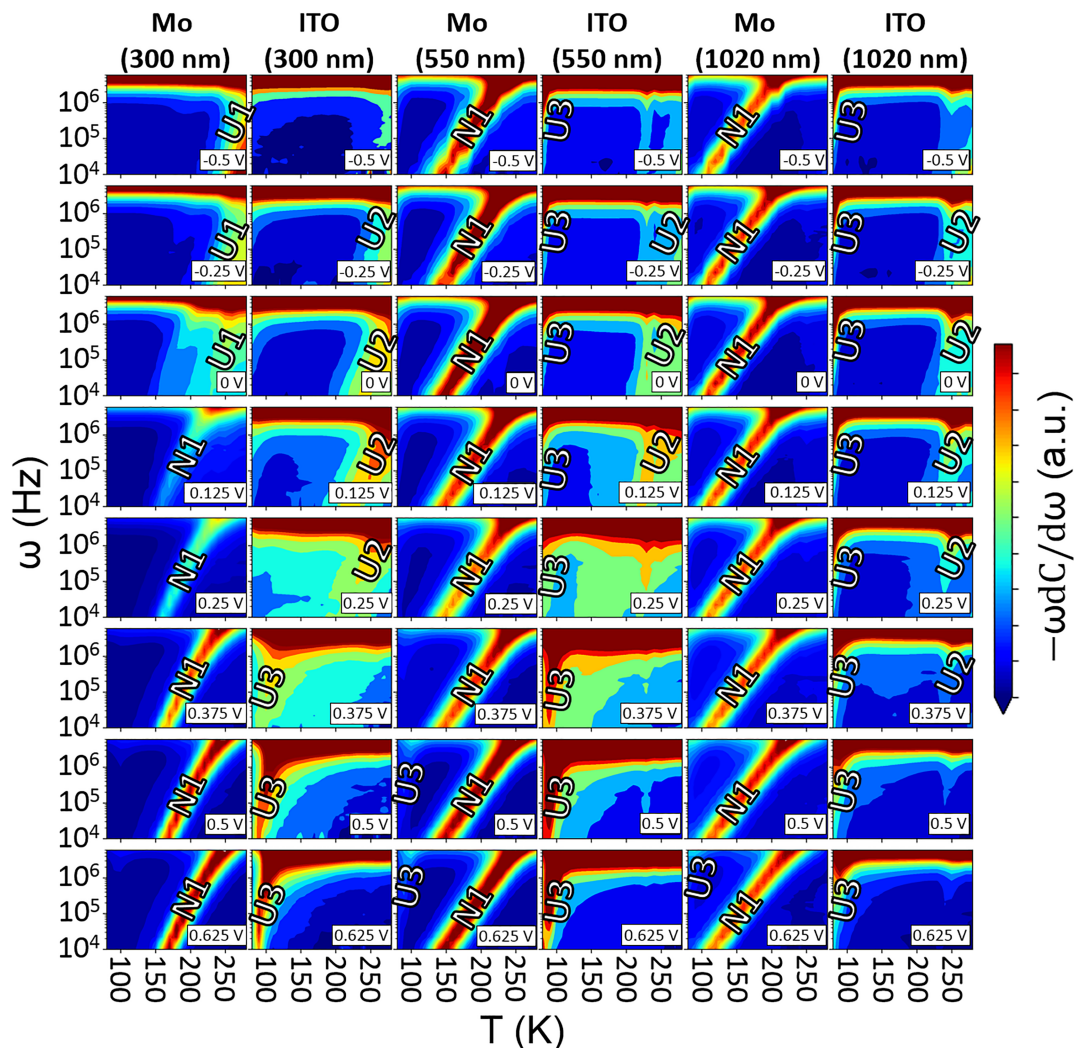
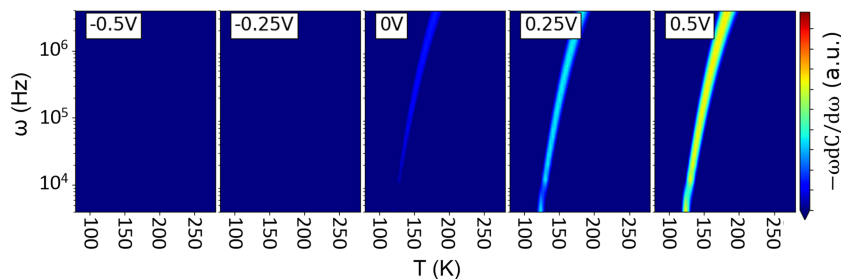


FIGURE 7 Color plot of $-\omega dC/d\omega$ as a function of temperature and angular frequency for the six samples at different bias voltages. Note that each plot has its own relative color scale

FIGURE 8 Simulated admittance spectra of a CIGSe solar cell with a 300-nm-thick absorber layer and a hole extraction barrier of 250 meV at the back contact



of a hole mobility being limited by acoustic deformation potential scattering ($\mu \sim T^{-1.5}$). Note that our evaluation differs from the expression in Eisenbarth et al.¹ The determined barrier heights given for the three samples in the order of ascending absorber thickness are 285 meV, 210 meV, and 175 meV. The determined barrier heights are therefore slightly above the values calculated from the V_{OC} versus T curves. Eisenbarth et al. found that the determined barrier height varied upon different sample treatments.⁴ For instance, there the sample

exhibited an N1 signal with an activation energy changing from about 160 meV in the relaxed (or reverse bias) state to about 40 meV in the white light soaked (or forward biased) state. The samples shown here were brought into the relaxed state only for admittance and dark JV measurements but were in the white light soaked state for the V_{OC} (T) measurement. Hence, the slightly lower activation energies found in the V_{OC} versus T measurements could be caused by a different sample state.

Considering the U1 and U2 signals, it is unlikely that they are caused by a back contact barrier, because an increased step height would be anticipated with increasing forward bias, as can be seen for the N1-signal in Figure S4. A possible explanation could be a bulk defect, where we tentatively assume both U1 and U2 to share the same origin. However, a determination of the activation energy was not possible, because no inflection point could be recognized in any of the measurements. The decrease of the capacitance at very low temperatures denoted as U3 is most likely caused by a freeze out of the majority carrier response. In this case, the capacitance should drop to the geometrical capacitance density of the absorber layer $C/A = \epsilon/d$ with ϵ being the dielectric constant, A the cell area and d the layer thickness. The calculated value is 40 nF/cm^2 for the 300-nm-thick absorber layer. The measured capacitance is approximately 25 nF/cm^2 for the ITO-based and even lower for the Mo-based sample. The effect is better visible at forward bias because the difference between the space charge region capacitance and the geometrical capacitance is larger in this case. It is more pronounced for the ITO-based samples due to the absence of the N1 signal. A possible explanation for the discrepancy between calculated and geometrical capacitances is that the geometrical capacitance at low temperatures is formed by the CIGSe, the CdS, and the i-ZnO layers with a total thickness of 480 nm.

3.6 | Microscopic properties of the back contact interfaces

The back contact barrier in the case of the Mo-based samples is related to a mismatch between the work function of the back contact and the Fermi energy of the absorber layer; that is, a Schottky contact is forming at the interface. Since it is known that a thin layer of MoSe₂ is forming during the evaporation of CIGSe on top of the Mo back contact,^{6,33,34-36} a barrier can principally be located at the MoSe₂/CIGSe interface, at the Mo/MoSe₂ interface, or at both interfaces. Based on the actual experimental findings, we cannot conclude the position of this barrier. The impact of Na incorporation on the contact resistance between CIGSe and Mo was studied by Yoon et al. by performing transmission line measurements on samples with different Na supply.³⁵ Samples without Na exhibited an approximately four times higher contact resistance compared with samples grown with Na incorporation. Similar results were obtained by Wada et al.⁶ Mirhosseini et al. performed DFT calculations to calculate the formation energy and the band alignment of the MoSe₂/Mo interface with different crystal orientations.³⁶ A Schottky barrier height of about 0.3 eV was found for a MoSe₂(0001)/Mo(110) interface, while it was only 0.01 eV for a MoSe₂ (11 $\bar{2}$ 0)/Mo(110) interface. Additionally, the influence of Na incorporation in the MoSe₂ was studied. A decrease of the Schottky barrier height upon Na incorporation was only observed in the calculations if Na occupied substitutional sites on Mo vacancies. The crystal orientation of MoSe₂ grown on Mo with and without the presence of Na was studied by various authors.^{6,33,34} In general, the c-axis of the MoSe₂ planes is oriented more parallel to

the Mo surface (like in the case of a MoSe₂ (11 $\bar{2}$ 0)/Mo(110) interface) when Na was absent during the growth process. In contrast, the c-axis is oriented more normal to the Mo surface (like in the case of a MoSe₂(0001)/Mo(110) interface) when Na was present during the growth. Hence the reduced contact resistance observed in CIGSe/Mo samples when Na was present during the growth can be explained by a better band alignment in case of the MoSe₂ (11 $\bar{2}$ 0) orientation possibly together with incorporation of Na in the MoSe₂. We therefore speculate that the scattering of activation energies of the N1 signal in our Mo-based samples results from different orientations of the MoSe₂ interface layer. In addition, minor differences in the sample treatment before the measurement may play a role.

The presence of a kink in low temperature JV measurements instead of a complete rollover could also be related to a MoSe₂ layer. Abou-Ras et al. investigated the thickness of MoSe₂ layers after the selenization of Mo covered substrates.³⁷ Only a very thin MoSe₂ layer was reported for process temperatures below 550°C. Furthermore, Na is reported to enhance the formation of MoSe₂.³³ Due to the low process temperature and the complete absence of Na during the layer growth in our case, a rather thin MoSe₂ layer can be expected. Assuming that the kink is caused by a breakdown of the diode at the back contact, this may be facilitated by the very low MoSe₂ thickness (alternatively tunneling between the absorber and the Mo may become possible). The carrier extraction in the case of the ITO back contact is not fully understood. For an n+ layer as back contact of a p-type solar cell, a counter diode hindering the current transport is expected, as can be seen in³⁸ for an AZO back contact. In contrast, often an ohmic contact is reported for CIGSe/TCO interfaces.⁹ ITO typically is highly doped, and according to UV-VIS measurements on the rear ITO presented in Schneider et al.,¹³ a degeneration of the ITO can be assumed. If now the p-doping of CIGSe in proximity to the back contact would be very high, the band bending at the interface will become very strong and even direct tunneling may become possible. A possible origin for high p-doping is

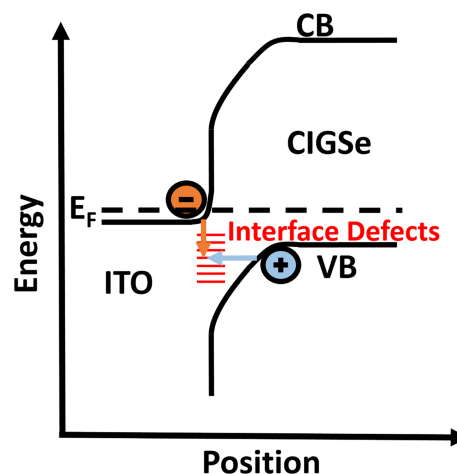


FIGURE 9 Schematic representation of a possible band diagram at the CIGSe/ITO back interface

the compensation of selenium vacancies (donors) by oxygen, which is available in the vicinity of a TCO-based back contact.³⁹ When a sufficiently high defect density is present in the vicinity of the back contact, a tunneling contact may form. Figure 9 shows a possible configuration of the CIGSe/ITO interface constructed with the help of band diagram calculations using AFORS-HET. Here, the doping density of CIGSe is 10^{16} cm^{-3} except for a 20 nm thick layer, which has a doping density of $2 \cdot 10^{18} \text{ cm}^{-3}$ in proximity to the ITO. The thin highly doped layer leads to a small upward band bending relative to the CIGSe bulk and in addition reduces the width of the space charge region at the back contact significantly. Such a space charge region would allow for tunneling transport of holes from the CIGSe to hypothetical interface defects as pointed out in Figure 9. The same holds for electrons from the ITO. As a result, a transport channel between ITO and CIGSe may form, which would explain the high short circuit current. Its reduction in the ITO-based solar cell with a 1,020 nm thick absorber layer could originate in a problem with carrier extraction in this sample possibly due to an oxide layer formed in the longer deposition period as compared to thinner CIGSe layers. However, further research is needed to clearly understand the carrier extraction mechanism in the ITO-based samples and the band diagram in the vicinity of the back contact.

4 | CONCLUSIONS

In this work, the back contact of CIGSe solar cells has been changed from Mo to ITO and the CIGSe absorber thickness has been varied. The devices were analyzed by temperature-dependent admittance and JV measurements. As usual for Mo-based samples, the $V_{OC}(T)$ plots exhibit a changing slope at lower temperatures and the well-known N1 defect appears in admittance spectroscopy. Both are absent for the ITO back contact. Since ITO and Mo samples otherwise have very similar properties, it is concluded that there is no blocking transport barrier at the ITO back contact. Furthermore, this comparison indicates that the N1 admittance signature in standard Mo-based solar cells indeed is due to a hole barrier as surmised before¹ but never proven independently. This interpretation is also compatible with the N1 voltage dependence in ultrathin Mo-based CIGSe devices. A model for charge transport over the p-CIGSe/n-ITO contact is proposed. However, details of this contact remain open such as a temperature dependent J_{SC} that is observed for increasing CIGSe layer thickness.

ACKNOWLEDGEMENT

The authors gratefully acknowledge funding through the Bundesministerium für Bildung und Forschung, Germany (BMBF) project StrukturSolar II (03EK3570B). Open Access funding enabled and organized by Projekt DEAL.

DATA AVAILABILITY STATEMENT

The data that support the findings of this study are available from the corresponding author upon reasonable request.

ORCID

Torsten Hölscher  <https://orcid.org/0000-0002-0690-484X>

Heiko Kempa  <https://orcid.org/0000-0003-3583-6935>

Roland Scheer  <https://orcid.org/0000-0001-5007-3425>

REFERENCES

- Eisenbarth T, Unold T, Caballero R, Kaufmann CA, Schock HW. Interpretation of admittance, capacitance-voltage, and current-voltage signatures in Cu (In, Ga) Se₂ thin film solar cells. *J Appl Phys*. 2010; 107(3):034509.
- Werner F, Wolter MH, Siebentritt S, et al. Alkali treatments of Cu (In, Ga) Se₂ thin-film absorbers and their impact on transport barriers. *Prog Photovolt*. 2018;26(11):911-923.
- Herberholz R, Igalson M, Schock HW. Distinction between bulk and interface states in CuInSe₂/CdS/ZnO by space charge spectroscopy. *J Appl Phys*. 1998;83(1):318-325.
- Eisenbarth T, Caballero R, Nichterwitz M, Kaufmann CA, Schock HW, Unold T. Characterization of metastabilities in Cu (In, Ga) Se₂ thin-film solar cells by capacitance and current-voltage spectroscopy. *J Appl Phys*. 2011;110(9):094506.
- Neugebohrn N, Hammer MS, Neerken J, Parisi J, Riedel I. Analysis of the back contact properties of Cu (In, Ga) Se₂ solar cells employing the thermionic emission model. *Thin Solid Films*. 2015;582:332-335.
- Wada T, Kohara N, Nishiwaki S, Negami T. Characterization of the Cu (In, Ga) Se₂/Mo interface in CIGS solar cells. *Thin Solid Films*. 2001; 387(1-2):118-122.
- Roussillon Y, Karpov VG, Shvydka D, Drayton J, Compaan AD. Back contact and reach-through diode effects in thin-film photovoltaics. *J Appl Phys*. 2004;96(12):7283-7288.
- Nakada T. Microstructural and diffusion properties of CIGS thin film solar cells fabricated using transparent conducting oxide back contacts. *Thin Solid Films*. 2005;480-481:419-425.
- Mollica F, Jubault M, Donsanti F, et al. Light absorption enhancement in ultra-thin Cu(In,Ga)Se₂ solar cells by substituting the back-contact with a transparent conducting oxide based reflector. *Thin Solid Films*. 2017;633:202-207.
- Kim K, Shafarman WN. Alternative device structures for CIGS-based solar cells with semi-transparent absorbers. *Nano Energy*. 2016;30: 488-493.
- Keller J, Chen W, Riekehr L, Kubart T, Törndahl T, Edoff M. Bifacial Cu (In, Ga) Se₂ solar cells using hydrogen-doped In₂O₃ films as a transparent back contact. *Prog Photovolt*. 2018;26(10):846-858.
- Keller J, Nilsson NS, Aijaz A, et al. Using hydrogen-doped In₂O₃ films as a transparent back contact in (Ag, Cu)(In, Ga) Se₂ solar cells. *Prog Photovolt*. 2018;26(3):159-170.
- Schneider T, Scheer R. Aluminum based back reflectors for ultrathin Cu(In,Ga)Se₂ solar cells with ITO diffusion barrier. Proceedings of the 36th European Photovoltaic Solar Energy Conference; 2019: 684-688.
- Schneider T, Tröndle J, Fuhrmann B, Syrowatka F, Sprafke A, Scheer R. Ultrathin CIGSe solar cells with integrated structured back reflector. *Solar RRL*. 2020;4(10):2000295.
- Gouillart L, Cattoni A, Goffard J, et al. Development of reflective back contacts for high-efficiency ultrathin Cu (In, Ga) Se₂ solar cells. *Thin Solid Films*. 2019;672:1-6.
- Bissig B, Carron R, Greuter L, et al. Novel back contact reflector for high efficiency and double-graded Cu (In, Ga) Se₂ thin-film solar cells. *Prog Photovolt*. 2018;26(11):894-900.
- Gouillart L, Cattoni A, Chen W, et al. Interface engineering of ultrathin Cu (In, Ga) Se₂ solar cells on reflective back contacts. *Prog Photovolt*. 2021;29(2):212-221.
- Schneider T, Hölscher T, Kempa H, Scheer R. Determination of the back contact recombination velocity of a Cu(In,Ga)Se₂/ITO interface

- using bifacial solar cells. Proceedings of the 37th European Photovoltaic Solar Energy Conference; 2020:621-626.
19. Varache R, Leendertz C, Gueunier-Farret ME, Haschke J, Muñoz D, Korte L. Investigation of selective junctions using a newly developed tunnel current model for solar cell applications. *Sol Energy Mater Sol Cells*. 2015;141:14-23.
 20. Cadel E, Barreau N, Kessler J, Pareige P. Atom probe study of sodium distribution in polycrystalline Cu (In, Ga) Se₂ thin film. *Acta Mater*. 2010;58(7):2634-2637.
 21. Villanueva-Tovar A, Kodalle T, Kaufmann CA, Schlatmann R, Klenk R. Limitation of current transport across the heterojunction in Cu(In,Ga) Se₂ solar cells prepared with alkali fluoride postdeposition treatment. *Solar RRL*. 2020;4(4):1900560.
 22. Ledinek D, Salomé P, Hägglund C, Zimmermann U, Edoff M. Rear contact passivation for high bandgap Cu (In, Ga) Se₂ solar cells with a flat Ga profile. *IEEE J Photovolt*. 2018;8(3):864-870.
 23. Burgelman M, Engelhardt F, Guillemoles JF, et al. Defects in Cu (In, Ga) Se₂ semiconductors and their role in the device performance of thin-film solar cells. *Prog Photovolt*. 1997;5(2):121-130.
 24. Ott T, Schönberger F, Walter T, et al. Verification of phototransistor model for Cu (In, Ga) Se₂ solar cells. *Thin Solid Films*. 2015;582:392-396.
 25. Nishimura T, Hamada N, Chantana J, et al. Application of two-dimensional MoSe₂ atomic layers to the lift-off process for producing light-weight and flexible bifacial Cu(In, Ga)Se₂ solar cells. *Appl Energy Mater*. 2020;3(10):9504-9508.
 26. Mavlonov A, Chantana J, Nishimura T, et al. Superstrate-type flexible and bifacial Cu (In, Ga) Se₂ thin-film solar cells with In₂O₃:SnO₂ back contact. *Solar Energy*. 2020;211:725-731.
 27. Scheer R, Schock H-W. *Chalcogenide Photovoltaics - Physics, Technologies, Thin Film Devices*. Weinheim: Wiley VCH; 2011.
 28. Sozzi G, Lazzarini M, Menozzi R, et al. A numerical study of the use of C-V characteristics to extract the doping density of CIGS absorbers: 2016 IEEE 43rd Photovoltaic Specialists Conference, Portland, OR, USA, 5-10 June 2016. IEEE; 2016:2283-2288.
 29. Cwil M, Igalson M, Zabierowski P, Siebentritt S. Charge and doping distributions by capacitance profiling in Cu (In, Ga) Se₂ solar cells. *J Appl Phys*. 2008;103(6):063701.
 30. Nicollian EH, Brews JR. *MOS (Metal Oxide Semiconductor) Physics and Technology*. Wiley Classics Library; 2003.
 31. Brammertz G, Kohl T, Wild JD, et al. Bias-dependent admittance spectroscopy of thin-film solar cells: Experiment and simulation. *IEEE J Photovolt*. 2020;10(4):1102-1111.
 32. Walter T, Herberholz R, Müller C, Schock HW. Determination of defect distributions from admittance measurements and application to Cu (In, Ga) Se₂ based heterojunctions. *J Appl Phys*. 1996;80(8):4411-4420.
 33. Abou-Ras D, Mukherji D, Kostorz G, et al. Dependence of the MoSe₂ formation on the Mo orientation and the Na concentration for Cu(In,Ga)Se₂ thin-film solar cells. *Mater Res Soc Symp Proc*. 2005;865:1-6.
 34. Würz R, Marrón DF, Meeder A, et al. Formation of an interfacial MoSe₂ layer in CVD grown CuGaSe₂ based thin film solar cells. *Thin Solid Films*. 2003;431-432:398-402.
 35. Yoon J, Kim J, Kim WM, et al. Electrical properties of CIGS/Mo junctions as a function of MoSe₂ orientation and Na doping. *Prog Photovolt: Res Appl*. 2014;22(1):90-96.
 36. Mirhosseini H, Kiss J, Roma G, Felser C. Reducing the Schottky barrier height at the MoSe₂/Mo(110) interface in thin-film solar cells: Insights from first-principles calculations. *Thin Solid Films*. 2016;606:143-147.
 37. Abou-Ras D, Kostorz G, Döbeli M, et al. Formation and characterisation of MoSe₂ for Cu (In, Ga) Se₂ based solar cells. *Thin Solid Films*. 2005;480-481:433-438.

38. Rostan PJ, Mattheis J, Bilger G, Rau U, Werner JH. Formation of transparent and ohmic ZnO: Al/MoSe₂ contacts for bifacial Cu (In, Ga) Se₂ solar cells and tandem structures. *Thin Solid Films*. 2005;480-481:67-70.
39. Cahen D, Noufi R. Defect chemical explanation for the effect of air anneal on CdS/CuInSe₂ solar cell performance. *Appl Phys Lett*. 1989;54(6):558-560.

SUPPORTING INFORMATION

Additional supporting information may be found in the online version of the article at the publisher's website.

How to cite this article: Schneider T, Dethloff C, Hölscher T, Kempa H, Scheer R. Comparison of Mo and ITO back contacts in CIGSe solar cells: Vanishing of the main capacitance step. *Prog Photovolt Res Appl*. 2022;30(2):191-202. doi: 10.1002/pip.3476

APPENDIX A

Figure S5 shows the Arrhenius plots from the admittance frequencies for the three Mo-based samples. The temperature dependence of the prefactor in the Arrhenius plot can be derived as follows.

The admittance of the equivalent circuit of two diodes in series is given by

$$\frac{1}{Y_{total}} = \frac{1}{G_J + i\omega C_J} + \frac{1}{G_C + i\omega C_C} \quad (A1)$$

with the total admittance Y_{total} , the measurement frequency $\omega = 2\pi f$, the conductivity G , and the capacitance C . Quantities with the subscript C refer to the back contact diode while variables with J are associated with the junction diode at the front. The admittance of the sample is evaluated using an equivalent circuit comprised of a capacitor and resistor in parallel:

$$Y_{total} = G_{total} + i\omega C_{total}. \quad (A2)$$

The measured value C_{total} can be linked to Equation A1 using a comparison of the imaginary part of both equations for Y_{total} . This leads to the following expression:

$$C_{total} = \frac{C_C G_J^2 + C_J G_C^2 + \omega^2 C_C C_J (C_C + C_J)}{(G_C + G_J)^2 + \omega^2 (C_C + C_J)^2} \quad (A3)$$

The admittance measurements are evaluated by a calculation of the critical frequency ω_0 , which is defined as

$$\omega_0 = \max \left(-\omega \frac{dC}{d\omega} \right). \quad (A4)$$

Applying Equation A4 to Equation A3 leads to

$$\omega_0 = \frac{G_J + G_C}{C_J + C_C} \quad (\text{A5})$$

which is the essential equation to obtain the barrier height ϕ_B because of the temperature dependence of $G_C \exp\left(\frac{q\phi_B}{kT}\right)$. Therefore ϕ_B can be determined from an Arrhenius plot.

The equation can be further simplified using the condition $G_J \ll G_C$, which is usually applicable if the JV curve is not limited by the conductivity of the back contact, leading to

$$\omega_0 = \frac{G_C}{C_J + C_C} \quad (\text{A6})$$

The Arrhenius plot requires the determination of the temperature dependence of G_J, C_C , and C_J . An expression for G_C can be obtained from the current of the Schottky diode J_C using

$$G_C = \frac{dJ_C}{dV_C} \quad (\text{A7})$$

where V_C denotes the voltage drop across the back contact. Several expressions can be found in the literature to describe J_C , which are based on different assumptions about the limiting factor for the current transport through the Schottky diode. Herein, the expression of the so-called diffusion theory is employed, which is given by

$$J_C = q\mu_p E_{max} N_V \exp\left(\frac{-q\phi_B}{kT}\right) \left[\exp\left(\frac{qV_C}{kT}\right) - 1 \right] \quad (\text{A8})$$

with the majority carrier mobility μ_p , the maximum of the electric field close to the Schottky diode denoted as E_{max} and N_V the effective density of states in the valence band. E_{max} can be expressed as

$$E_{max} = \sqrt{\frac{2q(\phi_i - V_C)N_A}{\epsilon_s \epsilon_0}} \quad (\text{A9})$$

containing the built-in voltage ϕ_i of the Schottky diode. Therefore, G_J can be derived as

$$G_J = q\mu_p N_V \exp\left(\frac{-q\phi_B}{kT}\right) \left(\frac{d}{dV_C} [E_{max}] \left[\exp\left(\frac{qV_C}{kT}\right) - 1 \right] + E_{max} \frac{d}{dV_C} \left[\exp\left(\frac{qV_C}{kT}\right) - 1 \right] \right) \quad (\text{A10})$$

with

$$\begin{aligned} \frac{d}{dV_C} [E_{max}] \left[\exp\left(\frac{qV_C}{kT}\right) - 1 \right] &= \frac{-2qN_A}{\epsilon_s \epsilon_0} \left(\frac{2q(\phi_i - V_C)N_A}{\epsilon_s \epsilon_0} \right)^{-\frac{1}{2}} \left[\exp\left(\frac{qV_C}{kT}\right) - 1 \right] \\ &= \frac{-2qN_A}{\epsilon_s \epsilon_0 E_{max}} \left[\exp\left(\frac{qV_C}{kT}\right) - 1 \right], \end{aligned} \quad (\text{A11})$$

$$E_{max} \frac{d}{dV_C} \left[\exp\left(\frac{qV_C}{kT}\right) - 1 \right] = E_{max} \frac{q}{kT} \exp\left(\frac{qV_C}{kT}\right). \quad (\text{A12})$$

Equation A10 can be further simplified under the assumption

$$\frac{2qN_A}{\epsilon_s \epsilon_0 E_{max}} \left[\exp\left(\frac{qV_C}{kT}\right) - 1 \right] \ll E_{max} \frac{q}{kT} \exp\left(\frac{qV_C}{kT}\right) \quad (\text{A13})$$

or equivalently

$$\frac{2N_A kT}{\epsilon_s \epsilon_0 E_{max}^2} \left[\exp\left(\frac{qV_C}{kT}\right) - 1 \right] / \exp\left(\frac{qV_C}{kT}\right) \ll 1 \quad (\text{A14})$$

Under the assumption $G_J \ll G_C$ only a small portion of the applied bias voltage will drop over the back contact. Inserting typical values ($N_A = 10^{16} \text{ cm}^{-3}, T = 200 \text{ K}, \phi_i = 0.2 \text{ V}, V_C = 0.01 \text{ V}, \epsilon_s = 13.6$) leads to 0.04 for the left-hand side of Equation A14, which is much smaller than 1. Hence it appears reasonable to neglect the contribution of $\frac{d}{dV_C} [E_{max}] \left[\exp\left(\frac{qV_C}{kT}\right) - 1 \right]$ in Equation A10 leading to the following expression for G_J :

$$G_J = q\mu_p N_V \exp\left(\frac{-q\phi_B}{kT}\right) E_{max} \frac{q}{kT} \exp\left(\frac{qV_C}{kT}\right) \quad (\text{A15})$$

The temperature dependence of the prefactor of the Arrhenius plot can be discussed using Equation (A15). The effective density of states is proportional to $T^{1.5}$. The temperature dependence of μ_p will depend on the specific sample and measurement temperature. C_C, C_J , and E_{max} possess all some temperature dependence. However, the temperature dependence of those quantities is generally very small, as will be confirmed later by simulations.

The temperature dependence of ω_0 can be expressed eventually as

$$\omega_0 = \xi(T) \cdot \exp\left(\frac{q(V_C - \phi_B)}{kT}\right) \text{ with } \xi(T) = \text{const} \cdot \mu_p(T) \cdot T^{-1} \quad (\text{A16})$$

where $\mu_p(T)$ represents the temperature dependence of the majority carrier mobility. In total the barrier height can be obtained by linear fitting of a $\ln(\omega_0 \cdot T / \mu_p(T))$ versus T^{-1} plot. The voltage drop on the back contact can be neglected as long as $G_J \ll G_C$ is valid.

The derived expression was tested by calculating temperature-dependent capacity-frequency curves using AFORS-HET. These curves were evaluated using an Arrhenius plot with the temperature dependence of Equation A16. The effective carrier densities N_{eff} and mobilities μ have been adapted for each temperature using $N_{eff} = N_{eff}(300 \text{ K}) \cdot T^{-1.5}$ and $\mu = \mu(300 \text{ K}) \cdot T^{-1.5}$ for both carrier types. The temperature dependence of the mobilities represents the case that the mobilities are limited by acoustic deformation potential scattering. The results are given in Figure A1 as a function of the Schottky barrier height. The maximum deviation between the actual and determined barrier height is 1% and therefore the derived prefactor appears to be valid and the temperature dependence of C_C, C_J and E_{max} can indeed be neglected. Despite originating from different effects, the analysis of defect contributions to the admittance spectra is quite similar to

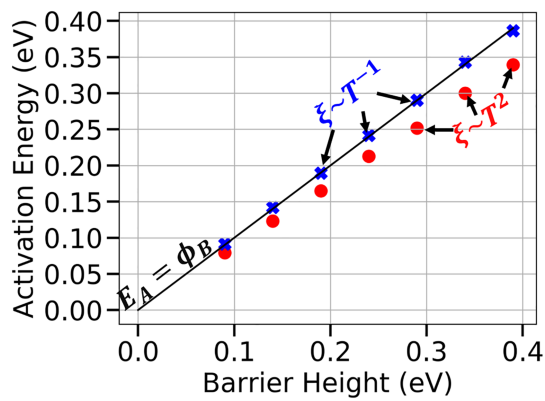


FIGURE A1 Determined activation energy E_a of solar cells with different Schottky barrier heights ϕ_B . The activation energies were obtained using an Arrhenius plot according to equation A16 from calculated capacitance-frequency curves. The crosses were calculated using a temperature-dependent prefactor of $\xi(T) = \text{const} * T^{-1}$ while the points are calculated using a prefactor of $\xi(T) = \text{const} * T^2$. The black line is plotted as a visual guide

the analysis for the determination of the back contact barrier height. The Arrhenius plot is constructed in the same way, with the only difference that the prefactor is $\xi(T) = \text{const} * T^2$. This factor is quite often used in the analysis of admittance spectra. Hence this temperature dependence was also added to Figure A1 in order to point out how much difference in the determined activation energy is obtained by using this prefactor. The relative deviation of the determined activation energy using this prefactor in relation to the barrier height is about 13% in all calculations.